ELSEVIER

Journal of Structural Geology 27 (2005) 2043–2057

JOURNAL OF STRUCTURAL GEOLOGY

www.elsevier.com/locate/jsg

# Dominant coaxial deformation of veins during the interseismic stage of the fault-valve cycle: microfabrics of laminated quartz veins of the Hutti gold mine, India

Jochen Kolb*, Amanda Rogers, F. Michael Meyer, Heinrich Siemes

*Institute of Mineralogy and Economic Geology, RWTH Aachen University, D-52056 Aachen, Germany*

Received 4 May 2004; received in revised form 3 June 2005; accepted 9 June 2005
Available online 1 August 2005

**Abstract**

Auriferous shear veins formed during greenschist facies reactivation of amphibolite facies shear zones of the Hutti mine. The laminated vein fabric, hydraulic breccias and fault gouge material formed by failure during the fault-valve cycle. Microstructural observations in the laminated quartz veins indicate that porphyroclasts of $quartz_1$, $scheelite_1$, and pyrrhotite have an oblate shape. $Quartz_2$ grains with a width of 0.03–0.05 mm result from predominant subgrain rotation, while predominant bulging recrystallization formed $quartz_2$ grains with a width of 0.01–0.03 mm. The pole figures of the quartz texture are symmetrical with respect to a shortening direction perpendicular to the vein walls. Strain partitioning of shear stress into the rheologically weaker altered host rocks preserved these fabrics in the stronger quartz veins. A non-coaxial overprint of the veins is only weakly recorded by the microfabrics and quartz textures. The study of microfabrics and quartz textures helps to understand processes of seismic activity in shear zones during fault-valve behavior. In the case of Hutti, coaxial deformation normal to the shear zone is indicated during the initial stages of shear stress and fluid pressure build-up, following the crack-seal stages.


*Keywords:* Quartz vein; Quartz texture; Microfabric; Fault-valve

## 1. Introduction

A great number of greenschist facies auriferous shear zones exhibit evidence for repeated transitions between brittle and ductile behavior related to fluid pressure and stress cycling (Cox et al., 1986, 1991, 2001; Sibson et al., 1988; Sibson, 1990, 2001; Boullier and Robert, 1992). Failure of a fault segment is caused by supralithostatic fluid pressure leading to highly permeable channel ways immediately post-failure. Porosities are created during episodic slip events by seismic deformation, whereas pore shrinkage and the loss of pore connectivity are due to hydrothermal precipitation. Fluid pressure recovery after the failure event can result in a cyclic repetition of the fault-valve process resulting in the formation of laminated quartz vein arrays. The interplay between vein formation, fluid pressure cycling and slip events during the reactivation of faults is relatively well understood however, the details of such interplay and the coseismic–interseismic periods during fault-valving are not very well known. Based on crack-seal structures, open-space filling textures and fluid inclusion characteristics, Boullier and Robert (1992) related the formation and collapse of horizontal extension veins to hydraulic fracturing and subsequent seismic slip along the fault.

Internal deformation features are an integral part of the progressive shear zone formation having developed during overprinting or reactivation of the quartz veins (Boullier and Robert, 1992; McCuaig and Kerrich, 1998; Robert and Poulsen, 2001). Thus, microstructural development of mineral fabrics and the crystallographic preferred orientation (CPO) of minerals are useful indicators of deformation characteristics of complex shear zones (e.g. Lister and Price, 1978; Lister and Snoke, 1984; Pryer, 1993; Lloyd and Freeman, 1994; Joy and Saha, 1998, 2000; Zulauf, 2001; Stipp et al., 2002; Kolb et al., 2003).

A model for the development of fluid conduits by seismic fracturing during fault-valve behavior of the auriferous

* Corresponding author. Tel.: +49 2418095773; fax: +49 2418092153.
*E-mail address:* kolb@rwth-aachen.de (J. Kolb).

0191-8141/$ - see front matter © 2005 Elsevier Ltd. All rights reserved.
doi:10.1016/j.jsg.2005.06.005

shear zones of the Hutti gold mine has been presented by Kolb et al. (2004). According to this, large laminated quartz vein sets were formed by a crack-seal-slip mechanism due to fluid pressure fluctuations, which is evidenced by the recognition of hydraulic breccias and fault-fill veins. To gain further knowledge about the structural evolution of the Hutti shear zones during the coseismic and interseismic stages of the fault-valve mechanism, this paper examines in detail quartz textures and microstructures of fault-fill veins and altered wall rocks. These data were used to describe the deformation style during the crack-seal-slip cycle at Hutti.

## 2. Regional geology

The Hutti gold mine is situated in the Archaean Hutti–Maski Greenstone Belt (HMGB) of the south Indian Dharwar Craton (Fig. 1). The hook-shaped HMGB consists of a heterogeneous assemblage of volcano-sedimentary lithologies (Riyaz Ulla et al., 1996; Vasudev et al., 2000). The stratigraphy of the greenstone belt remains unresolved because of the lack of any definite younging direction

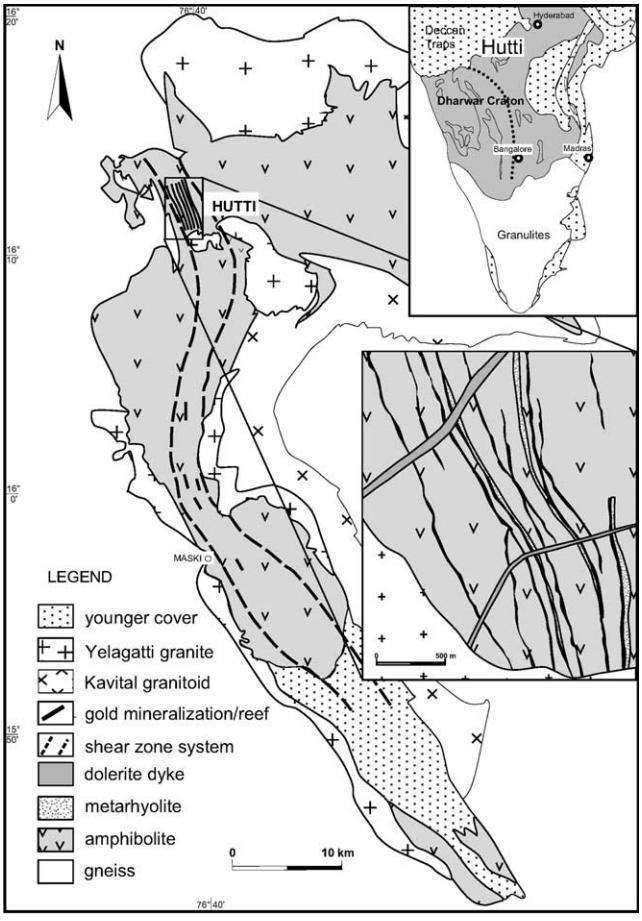


Fig. 1. Location of the study area in South India and geological map of the Hutti–Maski Greenstone Belt (modified after Srikantia, 1995). The inset shows the Hutti Gold Mine with the NNW–SSE-trending, anastomosing auriferous shear zones (reefs).

criteria. A granitoid pebble within a metaconglomerate yielded a SHRIMP weighted mean $^{207}Pb/^{206}Pb$ zircon age of $2576 \pm 12$ Ma, which is interpreted as the magmatic age of the provenance and, therefore, the maximum age of the belt (Vasudev et al., 2000). An upper intercept age of $2586 \pm 59$ Ma from SHRIMP U–Pb zircon dating of a metarhyolite gives a minimum age for felsic volcanism (Rogers, 2004). The western boundary of the HMGB is tectonically juxtaposed to gneisses, the northern, eastern, and southern contacts are intrusive. Two generations of intrusives can be distinguished, namely the Kavital and Yelagatti Granitoids (Srikantia, 1995). The syntectonic intrusion of the Kavital granitoid was dated at $2543.3 \pm 8.6$ Ma (SHRIMP U/Pb zircon discordia; Rogers, 2004).

### 2.1. Metamorphic conditions

The higher-grade metamorphic rocks of the HMGB are concentrated at the peripheral parts of the belt (Roy, 1979; Naganna, 1987; Riyaz Ulla et al., 1996; Vasudev et al., 2000). Peak conditions ($M_1$) recorded in amphibolites, the host rocks at Hutti, are $660 \pm 40$ °C and $400 \pm 100$ MPa (Pal and Mishra, 2002; Kolb et al., 2005). Amphibole and plagioclase rims yield retrograde conditions ($M_2$) at about $560 \pm 60$ °C and $200 \pm 100$ MPa (Kolb et al., 2005). Both amphiboles and plagioclase are replaced by chlorite and calcite, respectively, indicating a second retrogressive stage ($M_3$) at 300–400 °C and $<200$ MPa in the lower greenschist facies (Kolb et al., 2005). In addition, temperature and pressure estimates from fluid inclusion analysis point to conditions of $<380$ °C and $<320$ MPa for the $M_3$ stage (Pal and Mishra, 2002; Pandalai et al., 2003; Rogers, 2004).

### 2.2. Structure and conditions of deformation

At Hutti, five stages of deformation ($D_{1-5}$) can be distinguished (Kolb et al., 2004, 2005). During $D_1$ cm-scale quartz veins were formed by metamorphic segregation parallel to an $S_1$ foliation. The major N–S- to NNW–SSE-trending, shear zones at the western margin of the HMGB formed during ductile $D_2$ deformation (Fig. 1). A closely spaced $S_2$ foliation and rare quartz veins are restricted to the extent of the discrete shear zones, which dip steeply to the west. Sense of shear could not be determined due to the strong overprint by later deformation events and limited outcrop in the underground workings. The $D_3$ event is characterized by oblique shearing with respect to $D_2$ structures creating a $S_2$–$S_3$ asymmetric crenulation cleavage as well as large quartz vein arrays (Figs. 2 and 3). The sense of deformation is dextral strike- to oblique-slip. The later deformation events are characterized by kink bands and/or quartz–chlorite–calcite veins ($D_4$) and faults ($D_5$). Gold mineralization at Hutti is controlled by the NNW–SSE-trending, high-angle, $D_2/D_3$ shear zones, locally referred to as ‘reefs’ (Fig. 1; Naganna, 1987; Kolb et al., 2004, 2005).

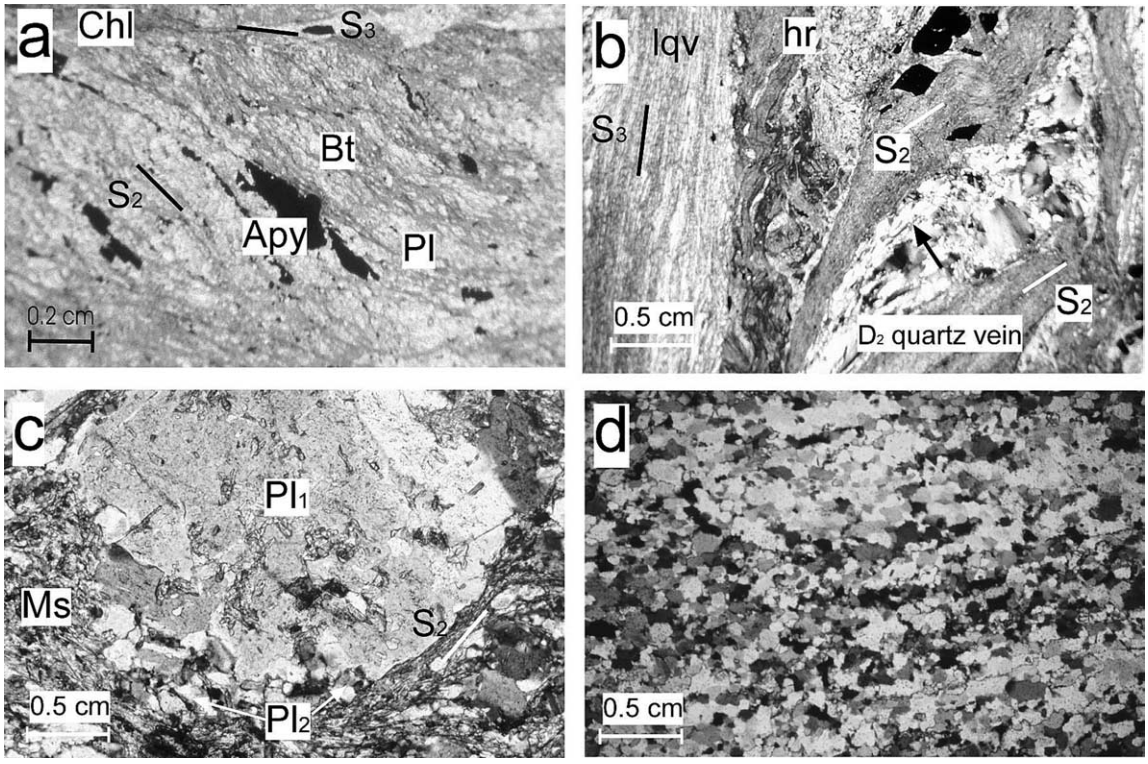


Fig. 2. Photomicrographs of $D_2$ fabrics. (a) Asymmetric $S_2$–$S_3$ crenulation cleavage with biotite (Bt), plagioclase (Pl), and arsenopyrite (Apy) in the $S_2$ domain (lithon), retrogressed by chlorite (Chl) along $S_3$ (plain polarized light). (b) Sigmoidal $D_2$ quartz vein developed parallel to $S_2$ in the altered host rock (hr). Note the $S_3$ parallel quartz fabric in the laminated quartz vein (lqv). The relatively large quartz grains in the $D_2$ vein are recrystallized by bulging during the retrograde $D_3$ overprint (arrow; crossed polarized light). (c) Plagioclase porphyroclast ($Pl_1$) dynamically recrystallized to $Pl_2$. Muscovite defines the $S_2$ foliation (crossed polarized light). (d) Quartz fabrics of the $D_2$ quartz vein from sample IH 24. The quartz grains are equigranular and have slightly undulating grain boundaries, which are the result of the greenschist facies $D_3$ overprint.

### *2.3. Evolution of the HMGB*

Radiometric age dating of schist belt lithologies limits the tectonometamorphic evolution of the HMGB to ages of less than about 2.58 Ga. Peak metamorphism under mid amphibolite facies conditions occurred contemporaneous with $D_1$ deformation (Kolb et al., 2005). Retrograde metamorphic stages followed a clockwise *P–T–t* path with $M_2/D_2$ in the lower amphibolite facies and $M_3/D_3$ in the lower greenschist facies. The latter stage overprinted the HMGB lithologies at about 2.55 Ga, as evidenced by the syntectonic Kavital granitoid. SHRIMP U/Pb dating of zircons from $D_4$ veins point to a Meso-Proterozoic overprint at about 1.2 Ga by brittle veining and faulting (Rogers, 2004).

## 3. Geology of the auriferous $D_2/D_3$ shear zones

Nine parallel shear zones can be distinguished, which show an anastomozing and undulating geometry, both down-dip and along strike (Fig. 1). Discrete shear zones may bifurcate to form two separate shear zones in down-dip and strike extension. These individual shear zones are up to 10 m wide and characterized by a mylonitic $S_2$ foliation, which dips steeply (60–85°) to the west. They are separated by up to 200-m-thick successions of relatively undeformed amphibolites and tabular bodies of metarhyolite. The $D_2$ shear zones have been reactivated during $D_3$ leading to a complex internal structure both on an outcrop- and a mine-scale (Kolb et al., 2004).

### *3.1. $D_2$ structures and petrography*

The outcrop of $D_2$ structures without any later overprint is very limited in underground exposure, because $D_3$ is the main gold-stage and those sections lacking $D_3$ structures are not mined. Relic $D_2$ structures are preserved in macro- and micro-lithons of the crenulation cleavage containing the earlier $S_2$ fabric (Fig. 2a and b). The scale of the lithons varies between 1 mm and 20 cm. Distinct mineralogical zoning comprises a 1.5-m-wide distal chlorite–sericite ($\pm$biotite, calcite, arsenopyrite, pyrite, gold) and a 3–5-m-wide proximal biotite–plagioclase ($\pm$quartz, epidote, calcite, arsenopyrite, pyrite, gold) alteration halo (Kolb et al., 2005). Chlorite, sericite, biotite, arsenopyrite, and epidote define the $S_2$ foliation. Locally, cm-scale quartz veinlets are developed parallel to $S_2$ (Fig. 2b and d). Plagioclase forms mantled porphyroclasts indicative of dynamic recrystallization of the feldspars during $D_2$ (Fig. 2c). In places, biotite

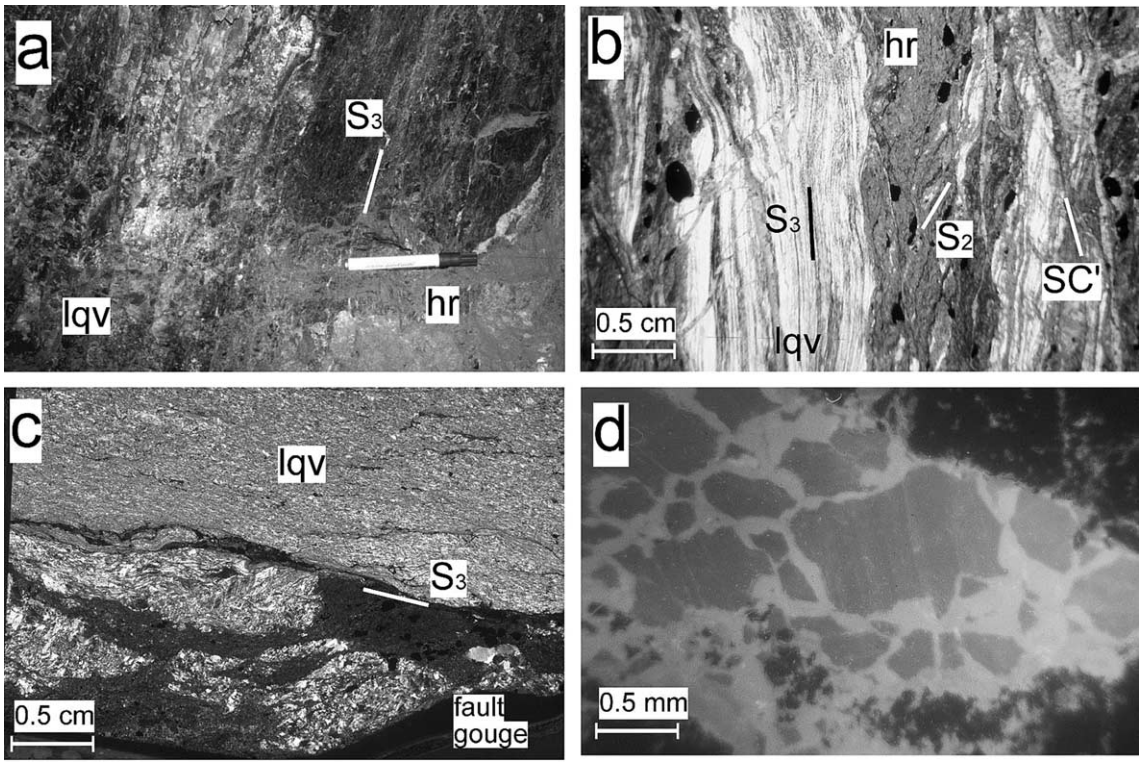


Fig. 3. Photographs of $D_3$ fabrics. (a) Sharp contact between laminated quartz vein (lqv) and altered host rocks (hr). Note the centimeter-scale lamination of the vein parallel to $S_3$. (b) Contact of quartz vein lamina and adjacent host rock showing the penetrative $S_3$ foliation, small lithons with $S_2$–$S_3$ crenulations and SC′ fabrics (crossed polarized light). (c) Very fine grained fault gouge material with $S_3$ foliation overprinting the laminated quartz vein (crossed polarized light). (d) Cathodoluminescence image showing a jigsaw puzzle or mosaic breccia of calcite and non-luminescent alteration minerals cemented by calcite from the direct contact of altered wall rock with a laminated quartz vein.

and sericite overgrow the $S_2$ foliation. The strong alteration of the host rocks together with the calculated mass balance (i.e. volume and mass increase of 10–20%) suggests intense fluid flow through a grain-scale mesh-like conduit during ductile $D_2$ shearing (Kolb et al., 2004).

### 3.2. $D_3$ structures and petrography

In the shear bands of the $S_2$–$S_3$ crenulation cleavage, chlorite, sericite, and tourmaline define the $S_3$ foliation replacing biotite (Fig. 2a). The asymmetric crenulation cleavage and $D_3$ S–C′ fabrics together with a sub-horizontal stretching lineation point to a dextral strike-slip sense of shear (Fig. 3). Zones of intense ductile $D_3$ shearing are marked by the inner chlorite–K-feldspar alteration assemblage ($\pm$quartz, calcite, tourmaline, titanite, zoisite, sericite, scheelite, pyrrhotite, chalcopyrite, sphalerite, arsenopyrite, ilmenite/rutile, and gold) (Kolb et al., 2005). This distinct alteration zone and the $S_3$ foliation are most prominent in close proximity to laminated quartz veins. Dimensions of the vein systems may attain maximum strike lengths of 250 m, down-dip extensions of 90 m, with widths up to 10 m (Kolb et al., 2004). The average size is 30–50 m along strike as well as down-dip, and 2–6 m in width. The laminated vein systems have a distinct internal structure and are composed of individual 4–10-cm-wide quartz veinlets alternating with mm-scale vein-fringing selvages of altered wall rock (i.e. inner chlorite–K-feldspar alteration; Fig. 3). The minimum strike and down-dip extent of individual laminated veins is about 3 m. The contact between the veins with the enveloping alteration assemblage is always sharp and parallel to the $S_3$ foliation. The selvages are locally characterized by a hydraulic breccia and/or very fine-grained fault gouge material (Fig. 3c and d). This material consists mainly of sub-microscopic calcite, chlorite and minor quartz, albite, K-feldspar, arsenopyrite, and pyrite, revealed from X-ray diffraction analysis of two samples. The hydraulic breccias show the typical jigsaw puzzle or mosaic fabric, with no evidence of rotation or large-scale translation (Fig. 3d).

The formation of the laminated quartz veins as fault-fill or shear veins parallel to the $S_3$ foliation is related to fault-valve action of the shear zones by repeated fluid pressure fluctuations during the change from brittle to ductile deformation mechanisms (Kolb et al., 2004). Ductile deformation resulted in the development of an asymmetric crenulation cleavage in the shear zone (Fig. 3b). Brittle deformation is manifested by the fault gouge, hydraulic breccia, and fault-fill veins, which are interpreted to having formed by hydraulic fracturing related to seismic slip events (cf. Sibson, 1986). The cyclic nature of the fault-valve process and progressive ductile and brittle deformation

explain the variable overprint of these structures (Fig. 3b and c).

Large fluid fluxes focused into the shear zones caused orthogonal or oblique extension and the formation of the fault-fill veins during $D_3$. No other form of brittle failure in the shear zones and within the adjoining intact rock mass is observed. This means that the fluid pressure ($P_f$) exceeded the sum of the local normal stress on the fault ($\sigma_n$) and the tensile strength of the fault rocks ($T_F$), but never exceeded the sum of the least principal stress ($\sigma_3$) and the tensile strength of the intact rock ($T$): $(\sigma_n + T_F) \leq P_f \leq (\sigma_3 + T)$ (Kolb et al., 2004). This suggests that the prevailing stress field during dextral strike-slip $D_3$ deformation and quartz veining was favorably oriented for reactivation of the $D_2$ shear zones, which limits the orientation of the mean principal stress $\sigma_1$, during $D_3$ to NNE–SSW directions. The least principal stress $\sigma_3$ is oriented NNW–SSE and $\sigma_2$ is almost vertical.

## 4. Analytical procedure

The samples investigated here were taken from four different, mineralized shear zones in underground exposures from the 22nd level of the Hutti mine. The microfabrics of laminated quartz veins were studied in oriented thin sections cut perpendicular to the $S_3$ foliation as well as perpendicular and parallel to the stretching lineation (i.e. the *XZ* and *YZ* sections of the finite strain ellipsoid). Measurements of long and short axes of quartz porphyroclasts as well as recrystallized quartz were performed using a microscope with an attached mechanical stage and a cross bar micrometer directly on the oriented thin sections. From this data, the *X*/*Z* and *Y*/*Z* aspect ratios of quartz porphyroclasts and recrystallized quartz were calculated. It should be noted that these measurements cannot represent the true grain size of the porphyroclasts due to misorientation of the thin sections with respect to the three-dimensional grain geometry and serrated grain boundaries. However, the measurements can be used to qualify grain shapes. The mean grain size of the recrystallized quartz was determined using the harmonic mean and standard deviation. Aspect ratios of recrystallized quartz are similar in *X*/*Z* and *Y*/*Z* sections and measurements are reproducible with an accuracy of about 1 μm.

Four samples from laminated quartz veins (IH 1, IH 29, IH 32, IH 59) were chosen for crystallographic preferred orientation (CPO) analysis. For comparison, the CPO of one $D_2$ quartz vein sample (IH 24) was also determined. Measurement of the pole figures was performed with a Philips PW 1710 X-ray structure goniometer using samples with an area of $13 \times 23$ mm and a thickness of 2–4.5 mm. The conditions for the Cu K$\alpha$ radiation were 35 kV, 30 mA, as well as usage of a Ni-filter. Step width was 5° in tilt $\Psi$ between 5 and 85°, and in azimuth $\Omega$. The poles measured include prism a {110} at 18.09° $\Theta$, prism m {100} at 10.27° $\Theta$, rhombohedral r and z {101} at 13.13° $\Theta$, and dipyramids {112} at 24.89° $\Theta$. The pole figures were corrected for defocusing by measurements of quartz powders with subsequent transformation and smoothing with the help of the program STARPLOT described by Traas et al. (1994). The orientation density function (ODF) was calculated from the measured and transformed pole figures using the computer program MENTEX (Schaeben and Siemes, 1996). The pole figures for {100}, {110}, {101}, and {112} were recalculated from the measured data set. The (001) pole figures were calculated using the data set of the four measured pole figures.

## 5. Petrography and microstructural development of the quartz veins

At the Hutti gold mine, four generations of quartz veins ($D_1$–$D_4$) can be distinguished. The more important $D_2$ and $D_3$ veins were analyzed in greater detail, because they are associated with the economic gold mineralization.

### 5.1. $D_2$ vein petrography and microstructures

The $D_2$ veins are 1–4 cm wide, up to 20 cm long and preferentially developed parallel to the $S_2$ foliation (Fig. 2b). They are composed of quartz and rare muscovite in places. Generally, only one generation of quartz grains is developed (Fig. 2d). They are mainly equigranular with diameters between 0.1 and 0.2 mm and show an undulose extinction with irregular grain shapes and grain boundaries, which is characteristic for the transition of subgrain rotation to grain boundary migration (cf. Drury and Urai, 1990; Stipp et al., 2002). In places, the quartz microfabric is equigranular polygonal suggesting complete recovery. The observed quartz fabric concurs well with the calculated *P*–*T* conditions of $560 \pm 60$ °C and $200 \pm 100$ MPa for $D_2$ and contemporaneous metamorphism (Kolb et al., 2005). The presence of muscovite may cause a general reduction of the quartz grain size. An overprint by lower greenschist facies $M_3$ metamorphism resulted in the local development of smaller quartz grains (0.05 mm), formed by subgrain rotation recrystallization from the older generation (Fig. 2b and d).

### 5.2. $D_3$ vein petrography and microstructures

The laminated veins are composed of quartz with minor calcite (average grain diameter: 120 μm), K-feldspar (~40 μm), scheelite, and muscovite (50 μm). The ore assemblage comprises pyrrhotite, chalcopyrite, arsenopyrite, and isolated grains of visible gold (up to 2 mm). Pyrrhotite forms elongate grains of up to 150 μm aligned parallel to the foliation. Chalcopyrite and arsenopyrite are less abundant and occur as rounded grains up to 60 μm in size. The laminated quartz veins are most productive in

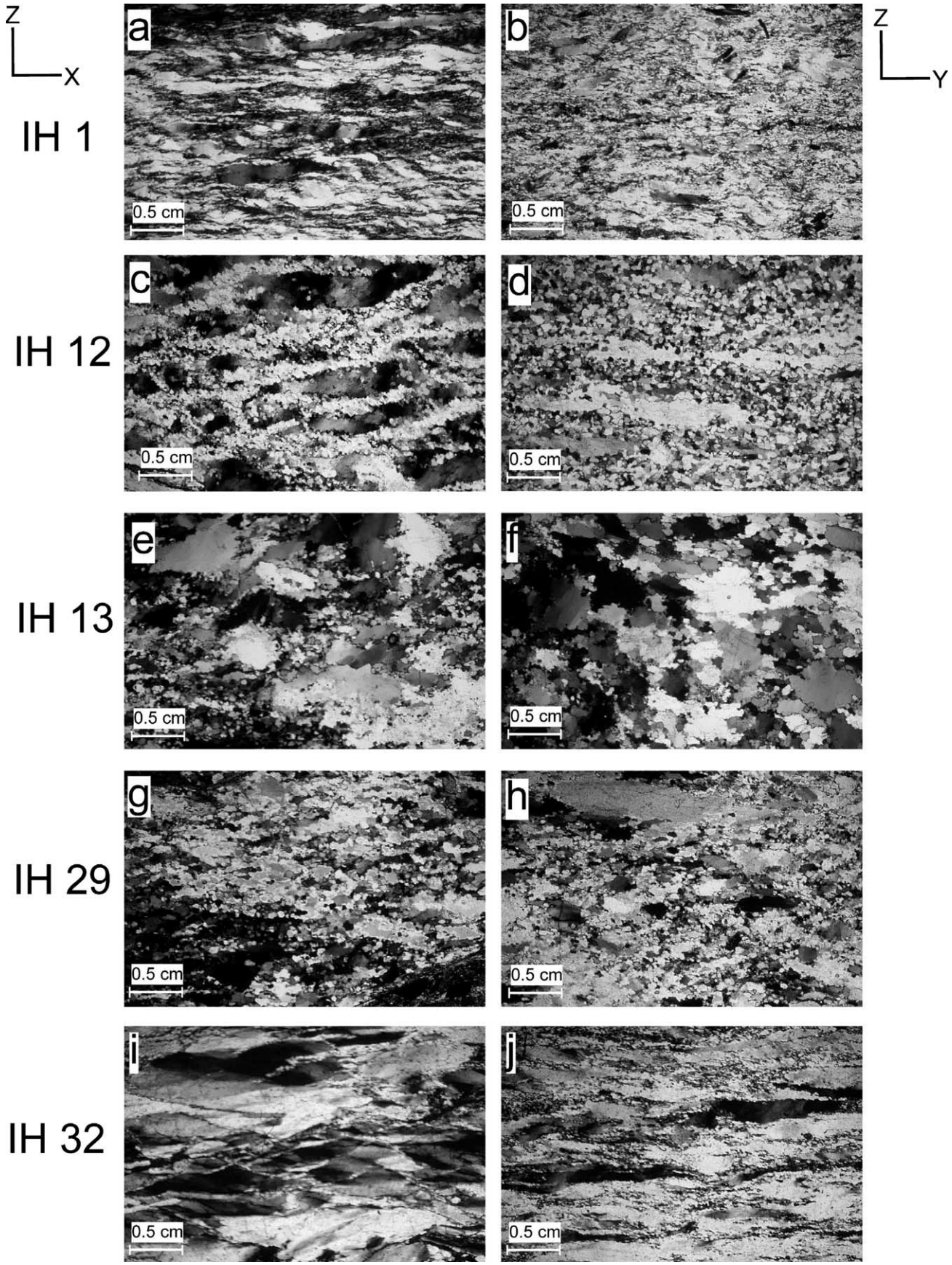
Z
X
Z
Y
IH 1
IH 12
IH 13
IH 29
IH 32
a
b
c
d
e
f
g
h
i
j
0.5 cm

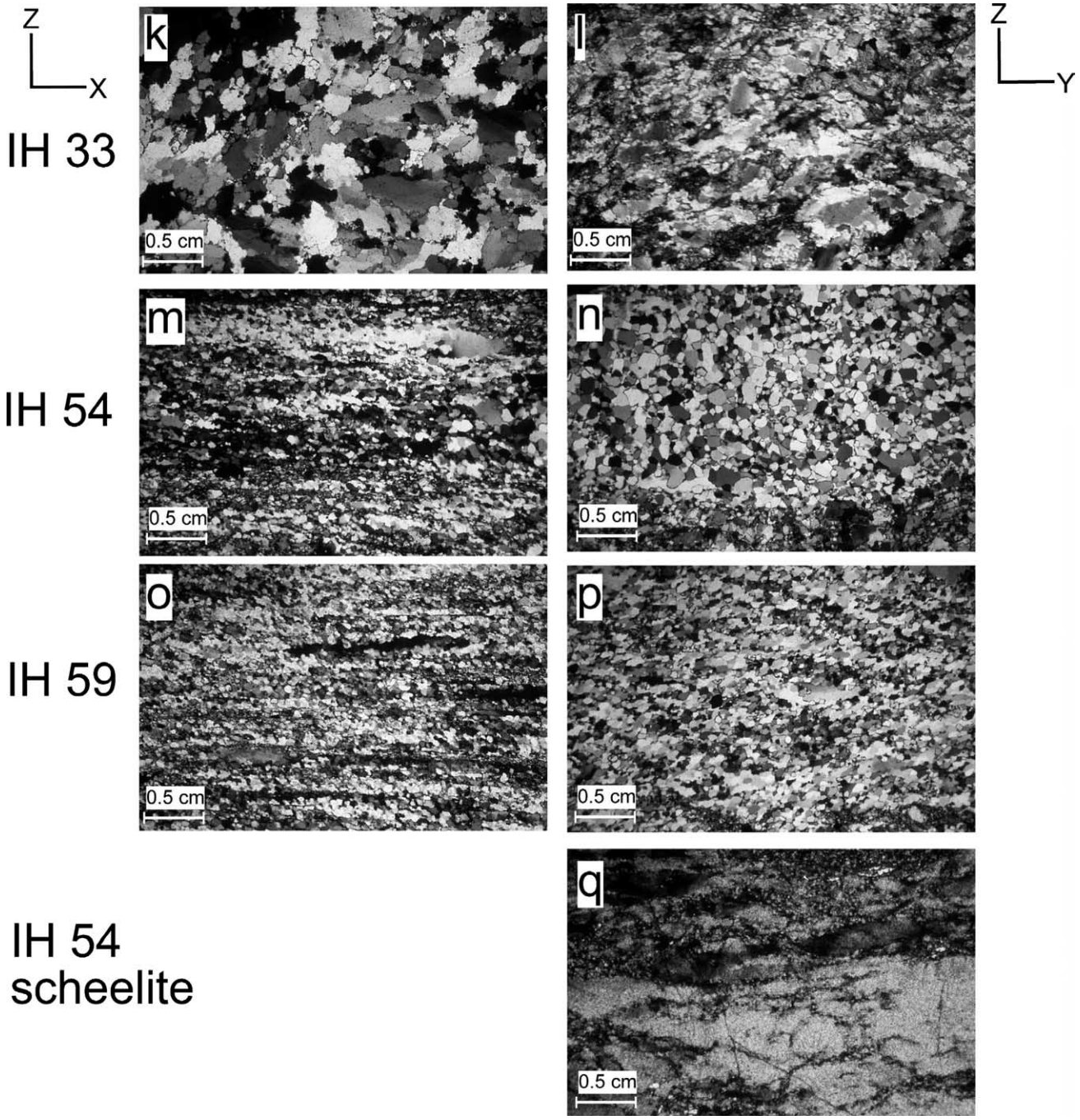


Fig. 4. Photomicrographs showing the quartz and scheelite microstructures in *XZ* and *YZ* sections (crossed polarized light, same magnification for all pictures). (a) and (b) Sample IH 1 with relatively large aspect ratios of quartz, porphyroclasts in *XZ* compared with *YZ*. Note the small $quartz_2$ grains rimming the porphyroclasts. (c) and (d) Sample IH 12 showing relatively strong subgrain development and recrystallization of $quartz_1$ by both subgrain rotation and bulging. (e) and (f) Sample IH 13 with almost equate $quartz_1$ porphyroclasts in *XZ* and *YZ* sections. Note the variably sized subgrains. Strongly serrated grain bulging recrystallization. (g) and (h) Sample IH 29 with a relatively strong recrystallized microstructure by both subgrain rotation and bulging. (i) and (j) Sample IH 32 shows similar $quartz_1$ porphyroclast aspect ratios in *XZ* and *YZ* sections. Recrystallization is weak mainly by bulging restricted to $quartz_1$ grain boundaries. (k) and (l) Sample IH 33 with relatively equate quartz porphyroclasts, which are only locally recrystallized at the grain boundaries. (m) and (n) Sample IH 54 has a weakly deformed and recrystallized microstructure with rare, small $quartz_2$ grains. (o) and (p) Sample IH 59 shows only relics of quartz ribbons in *XZ* sections. Note the smaller aspect ratios in *YZ*. Recrystallization by subgrain rotation is relatively strong. (q) Scheelite from sample IH 54 showing two generations: $scheelite_1$ porphyroclasts have large aspect ratios in the *YZ* section and are recrystallized by bulging along-grain boundaries and microshears to $scheelite_2$.

terms of gold and may contain up to 1 kg/t gold (pers. comm. mine geologists).

The microfabric of quartz varies strongly and two quartz generations can generally be distinguished (Fig. 4): $quartz_1$ forms variably sized porphyroclasts up to 3.5 mm long with undulose extinction as well as subgrains. Whereby two types of subgrains can be distinguished (Fig. 4c and e): (1) large, irregularly shaped subgrains (0.1–0.5 mm) and (2) subgrains, which are the same size as the recrystallized grains ($<$0.06 mm). The latter are mainly developed at the $quartz_1$ grain boundaries (Fig. 4a) or along microshears within the $quartz_1$ grains (Fig. 4i). Progressive deformation of the porphyroclasts leads to a grain size reduction and to quartz ribbons of more than 1 cm length in 2D view (Fig. 4o). The porphyroclast grain boundaries are strongly serrated.

The aspect ratios measured in $quartz_1$ porphyroclasts vary between 1.2 and 18.7 in *XZ* sections and between 1.7 and 13.3 in *YZ* sections. This data cannot accurately be described by mean values and standard deviation due to the strong spread of the aspect ratios, which reflects the problem of interpreting 3D grain shapes from 2D data (e.g. Heilbronner and Bruhn, 1998). However, for most of the samples the histograms of the measured aspect ratios in *XZ* and *YZ* sections overlap (Fig. 5). Only samples IH 1 and IH 59 show significant lower aspect ratios in *YZ* sections than in *XZ* sections. The relatively high *YZ* aspect ratios measured in sample IH 32 are explained by the sample heterogeneity. The $scheelite_1$ porphyroclast aspect ratios measured in sample IH 54 show a similar spread compared with $quartz_1$, suggesting similar grain shapes of the porphyroclasts (Fig. 5). The spread of the data is interpreted to result from the 3D geometry of the grains and the different position of the 2D sections in the $quartz_1$ porphyroclasts. Taking this into account, the similarity in the distribution of the aspect ratio data from *XZ* and *YZ* sections, respectively, suggests a discus-like or oblate 3D shape of the $quartz_1$ and $scheelite_1$ porphyroclasts.

The recrystallized $quartz_2$ grains occur in two distinct types (Figs. 4 and 6): Type 1 consists of 0.03–0.06 mm $quartz_2$ grains with relatively straight grain boundaries, which occur at $quartz_1$ grain boundaries and along microshears within the grains. Type 2 is represented by 0.01–0.03 mm $quartz_2$ grains developed at strongly bulged $quartz_1$ grain boundaries. Type 1 grains are not developed in samples IH 1, IH 33, and IH 54 (Fig. 6a, f and g), which indicates that in these samples quartz recrystallization occurred mainly by grain boundary bulging. In samples IH 29 and IH 59, the bimodal distribution of the $quartz_2$ grain sizes (Fig. 6d and h) are indicative of both bulging recrystallization and subgrain rotation. These recrystallization fabrics of quartz developed during $D_3$ are characteristic for lower to mid greenschist facies conditions (300–400 °C; cf. Drury et al., 1985; Drury and Urai, 1990; Zulauf, 2001; Stipp et al., 2002).

As scheelite occurs as a gangue phase in the quartz veins, some grains were also measured for comparison (Fig. 4q; IH 54). Similar to quartz, scheelite is also characterized by the presence of two distinct generations. Porphyroclasts show similar aspect ratios as the $quartz_1$ grains and also an oblate shape. Recrystallized scheelite is developed at strongly bulged $scheelite_1$ grain boundaries with an average grain size of 0.024 mm and is slightly larger than $quartz_2$ in the same sample (Fig. 6g). As the scheelite microfabric is similar to that observed for quartz, this also indicates bulging recrystallization of the mineral during $D_3$ at lower to mid greenschist facies conditions (300–400 °C).

## 6. Description of pole figures

Pole figure data for $D_2$ and $D_3$ quartz veins are presented in relation to the strain ellipsoid axes (Fig. 7). The *X*-axis lies parallel to the stretching lineation, *Z* is perpendicular to foliation and *Y* perpendicular to *X* and *Z*. The samples were prepared in *XZ* orientation with respect to $D_3$ structures.

### 6.1. $D_2$ vein quartz texture

The $D_2$ vein sample (IH 24) was chosen for texture analysis in order to compare it with the textures from the $D_3$ veins, to evaluate the degree of reactivation, and to gain additional information on the $D_2$ deformation characteristics. However, a problem arose with respect to the orientation of the sample, because no $D_2$ mineral stretching lineation could be defined. The sample was, therefore, oriented with respect to the strain ellipsoid axes of $D_3$. The calculated poles for (001), i.e. the *c*-axes, exhibit a transitional pattern between a crossed girdle distribution and two single maxima at about 30° to *Y* (Fig. 7). The pole figures for the prism and the rhombohedral planes display a consistent pattern with a maximum in *Y* and distribution at the periphery of the pole figure. One of the *a*-axis maxima is located parallel to the $D_3$ stretching lineation in *X*.

### 6.2. Quartz texture in $D_3$ veins

Four samples were chosen from the $D_3$ veins, which were affected by different types of recrystallization mechanisms and record variable grain shapes of porphyroclasts (Fig. 4) as is reflected by the distinct pole figures for the samples (Fig. 7).

#### 6.2.1. Samples IH 1 and IH 32

The two samples are dominated by strongly elongated $quartz_1$ porphyroclasts with serrated grain boundaries. Recrystallization occurred mainly by grain bulging. The major differences are that in sample IH 32 recrystallization by subgrain rotation is stronger and the porphyroclasts are larger (Fig. 4a/b, i/j). The pole figures of the two samples are also similar (Fig. 7). The poles of (001) display a transitional pattern between type I crossed girdles and a small circle

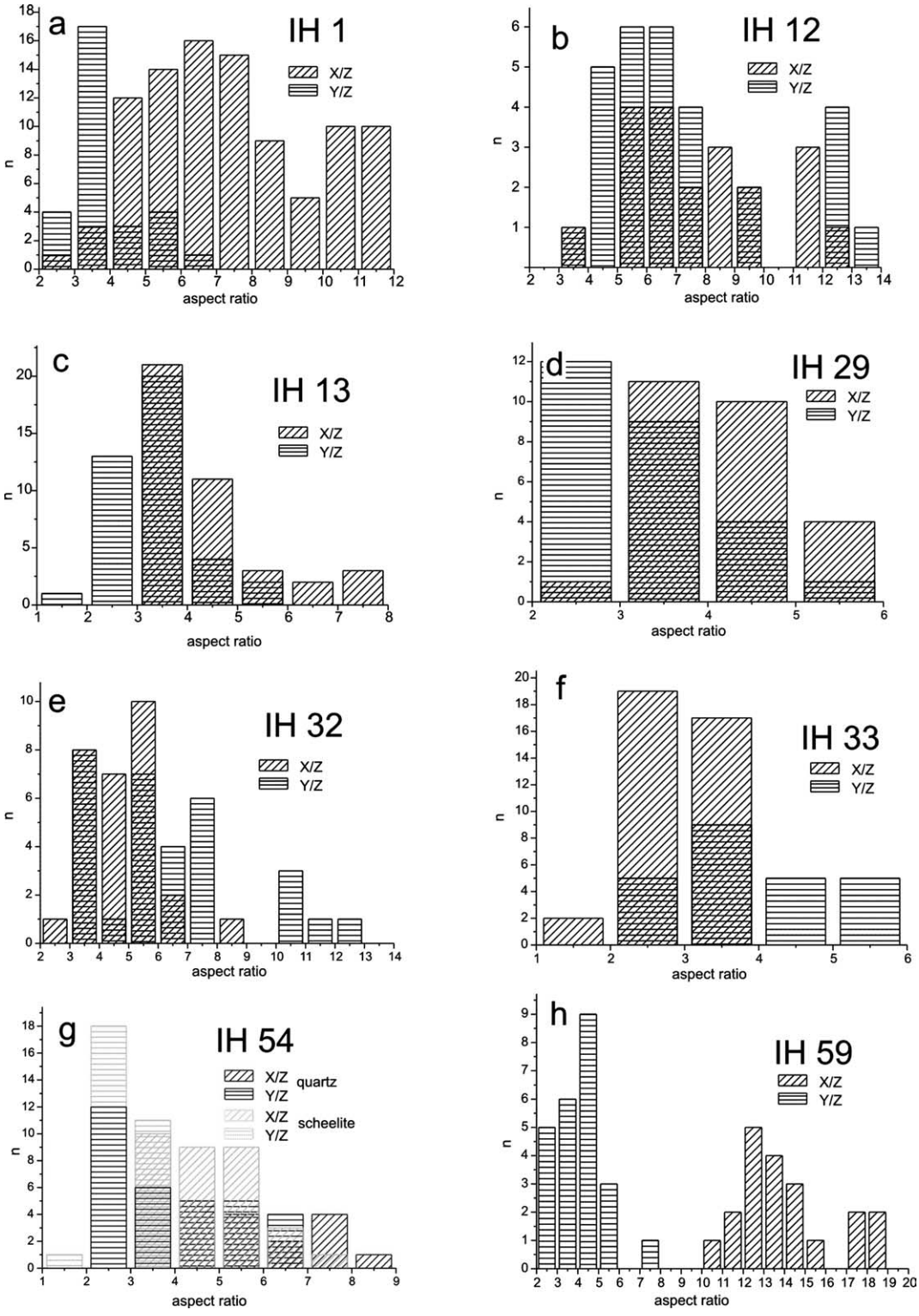


Fig. 5. Histograms for the measured *XZ* and *YZ* aspect ratios of quartz$_1$ porphyroclasts in different samples from laminated quartz veins. The similarity of the spread in the data is interpreted to reflect oblate 3D grain geometry.

pattern around *Z* (cf. Lister, 1977; Schmid and Casey, 1986). The pole figures of the prism planes exhibit a high angle small circle distribution around *Z*, with a maximum near *X* for the *a*-axis. The poles of {101} and {112} have a high angle small circle distribution around *X*. The pole figures of (001), {110} and {100} are slightly asymmetric to the selected *XYZ* reference frame.

### 6.2.2. Sample IH 29

This sample is characterized by intense recrystallization

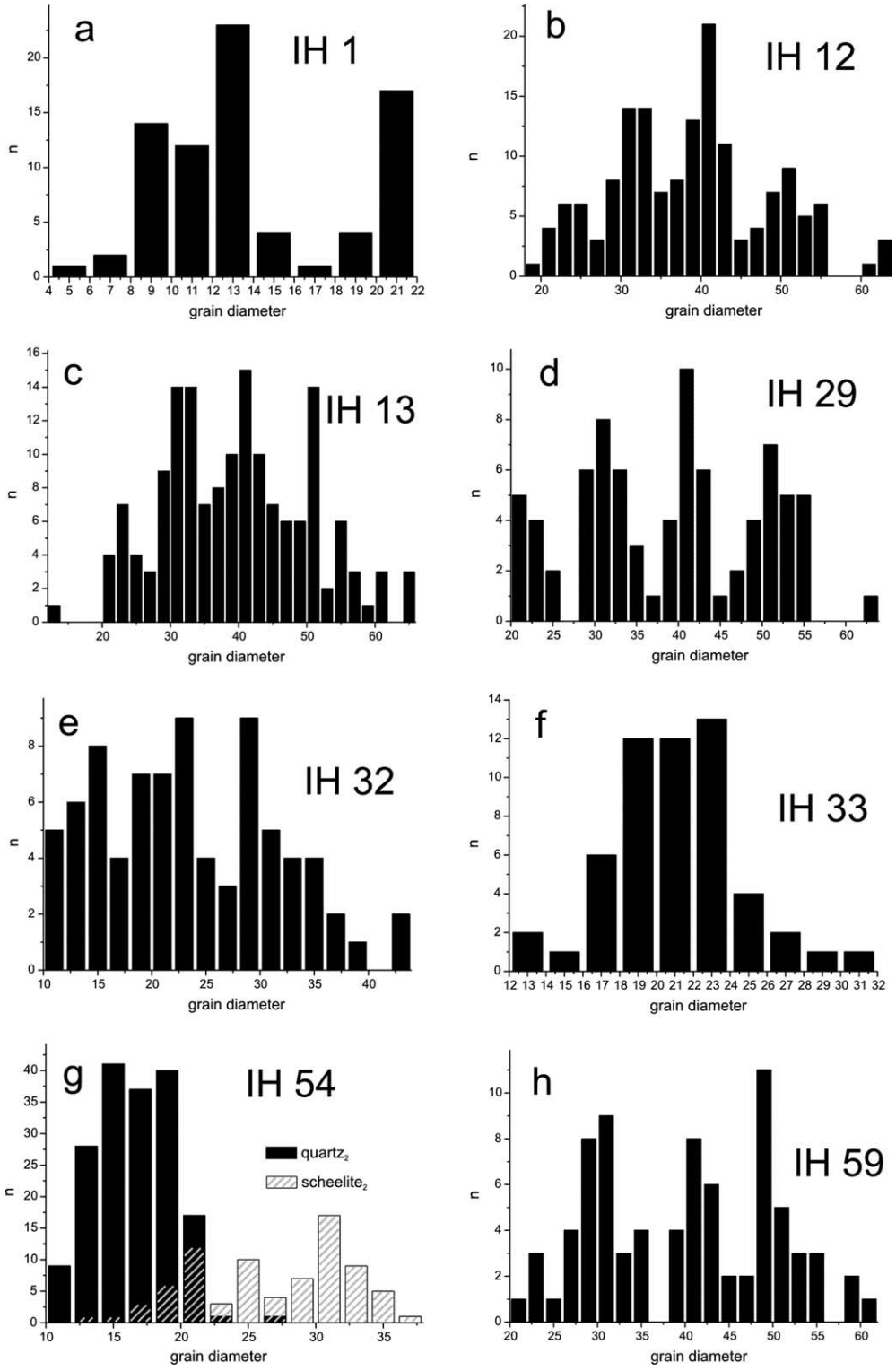


Fig. 6. Histograms for the measured grain size (in micrometers) of recrystallized quartz$_2$ in different samples from the laminated quartz veins.

of quartz$_1$ porphyroclasts by bulging and a significant amount of subgrain rotation (Fig. 4g and h). The (001) pole figure displays a transitional pattern between a small circle distribution around $Z$ and two single maxima at about 40° to $Y$ (Fig. 7). The poles of the prism planes exhibit two maxima near the $X$ direction with a tendency to spread along high angle small circles. The poles of {101} and {112} are consistent but do not display a strong preferred orientation.

### 6.2.3. Sample IH 59

Sample IH 59 is dominated by quartz$_2$ grains mainly formed by subgrain rotation (Fig. 4o and p). Rare quartz$_1$

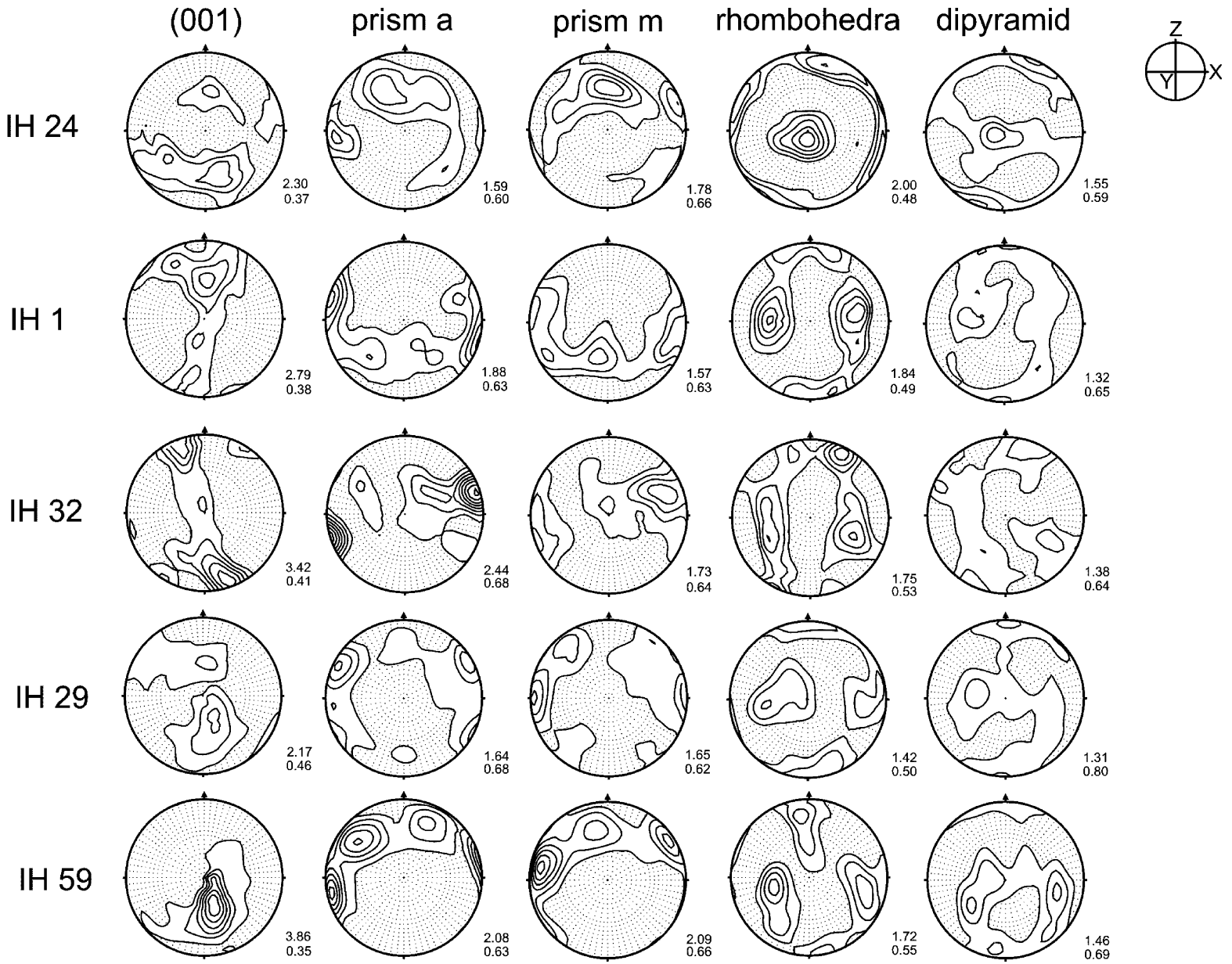


Fig. 7. Calculated and recalculated pole figures as contour plots in equal area lower hemisphere projections. The maximum and minimum densities in multiples of uniform expectation are given below each pole figure. Contour intervals are 0.5 for (001) and 0.2 for all other pole figures. Sample IH 24 represents a lower amphibolite facies $D_2$ quartz vein, whereas samples IH 1, IH 29, IH 32, and IH 59 are lower greenschist facies, laminated quartz veins formed during $D_3$. Note the tendency of poles to (001) and prism a planes to display small circle patterns around *Z* and *X*, respectively.

porphyroclasts are strongly elongated. The (001) pole figure shows a relatively strong maximum at about 30° to *Y* in the southern half (Fig. 7). The poles to {110}, {101}, {112}, and {100} have three maxima and form a consistent pattern. The most intense maxima for poles of the prism planes lie close to *X* pointing to ⟨a⟩ directed slip (Bouchez, 1978; Schmid and Casey, 1986).

## 7. Discussion

The microstructure and CPO of quartz yields information about the active slip mechanism, the grain shape, and the kinematic characteristics of deformation. The activation of the different slip systems in quartz is, in general, temperature sensitive (cf. Lister and Dornsiepen, 1982; Kruhl, 1996), however, water can have an effect in hydrolytic weakening of the quartz crystals and strain rate may also be important (e.g. Blacic, 1975; Lister and Dornsiepen, 1982; FitzGerald et al., 1991; Joy and Saha, 2000; Rutter and Brodie, 2004). In the following, we discuss the microstructure of the various laminated quartz vein samples and their CPO in order to identify deformation characteristics of the progressive formation and reactivation of the veins during $D_3$ and gold mineralization. Whether the textural and microstructural differences represent the coseismic–interseismic stages of the fault-valve cycle (sensu Sibson et al., 1988) is discussed.

The transitional character of the *c*-axis pole figures from a crossed girdle pattern to maxima at an intermediate orientation between the *Y*- and *Z*-axes is representative of deformation of quartz by a combination of different slip systems. Most of the pole figures show a preferred orientation for {110}, which points to the activation of slip systems, mainly in the ⟨a⟩ direction (Bouchez, 1978; Schmid and Casey, 1986). The *c*-axis maxima intermediate between *Y* and *Z* suggest that rhombohedral ⟨a⟩ slip was dominant, which is also in agreement with the preferred orientation of the rhombohedral planes. Notably, these *c*-axis maxima are most pronounced in samples with prevailing subgrain rotation recrystallization (i.e. IH 24, IH 29, IH 59). Samples IH 1 and IH 32 have *c*-axis maxima near *Z* suggesting a contribution by basal ⟨a⟩ gliding. The variation of CPO with bulging and subgrain rotation suggests that the reorientation of the quartz lattice is possibly controlled by the recrystallization mechanism. However, theoretical considerations contradict this suggestion (Lister and Price, 1978) and recrystallized grains commonly show only a slight variation in CPO compared with porphyroclasts resulting in a scatter of the pole figures (Stipp et al., 2002). The activated slip systems and the dominant recrystallization mechanism in these samples are characteristic for deformation between 300 and 400 °C (Voll, 1976; Lister and Price, 1978; Bouchez and Pêcher, 1981; Schmid and Casey, 1986; Lloyd and Freeman, 1994; Wenk, 1994; Zulauf, 2001), whereas Stipp et al. (2002) found temperatures >400 °C for dominant subgrain rotation recrystallization. The estimated *P–T* conditions from fluid inclusions (<380 °C, <320 MPa; Pal and Mishra, 2002; Pandalai et al., 2003; Rogers, 2004) and the uniformity of the alteration paragenesis spatially associated with the veins contradicts a formation at temperatures >400 °C as well as the possibility of significant temperature variations during quartz vein formation. The relatively small size of $quartz_2$ grains also suggests recrystallization under lower greenschist facies conditions (cf. Zulauf, 2001; Stipp et al., 2002), although the grain size is strongly dependent on strain rate and differential stress.

The development of different microstructures and textures can be explained in terms of strain heterogeneity due to variations in rheology (Blacic, 1975; Lister and Price, 1978; Lister and Dornsiepen, 1982). For the present study, samples were chosen from veins almost solely composed of quartz (Fig. 4). Therefore, strain heterogeneity is restricted to local discontinuities related to shape variations of primary quartz grains in the laminated quartz veins. Variations in strain rate are an integral feature of the fault-valve process and can, therefore, not be ruled out to account for the variable microstructures and textures in the laminated quartz veins.

Several authors point out that higher water contents possibly reduce the strength of the quartz crystals (Blacic, 1975; Lister and Dornsiepen, 1982; FitzGerald et al., 1991; Joy and Saha, 2000; Rutter and Brodie, 2004). In the case of Hutti, $D_3$ quartz veins formed during gold mineralization and hydrothermal alteration of the host rocks indicating high fluid–rock ratios. Fast grain growth, as can be expected for vein fillings, favors the incorporation of water into the quartz crystal lattice (Rutter and Brodie, 2004). Therefore, the effect of water can possibly explain the variations in microstructure and CPO of the different samples enabling subgrain rotation and rhombohedral ⟨a⟩ slip under lower temperature conditions. The change from subgrain rotation to bulging recrystallization of quartz was recently also interpreted by Mancktelow and Pennacchioni (2004) to represent dryer conditions.

### 7.1. Kinematic characteristics of deformation

The $D_2$ fabrics were strongly overprinted by the $D_3$ reactivation and, therefore, any kinematic information for $D_2$ is obscured (Kolb et al., 2004). The CPO of the $D_2$ vein sample IH 24 is distinctly different to those of the $D_3$ quartz veins (Fig. 7), which supports the interpretation of quartz vein formation during two different deformation events. The *a*-axis pole figure from sample IH 24 displays a maximum near the *X*-axis of the $D_3$ finite strain ellipsoid. This possibly suggests that the quartz CPO of the $D_2$ vein was modified by the $D_3$ stage of deformation due to reorientation of the quartz lattice by progressive crystal-plastic deformation (cf. Fig. 2b and d). The quartz CPO often preferably records the

last episode of deformation (Lister and Price, 1978; Joy and Saha, 2000); however, a definite interpretation from the analysis of only one sample is impossible.

All pole figures, including the $D_2$ sample IH 24, are not strictly symmetric to the chosen reference frame but show a rotation about *Y* of less than 10° (IH 24 less than 30°). This asymmetry is commonly attributed to non-coaxial deformation (Lister and Dornsiepen, 1982; Bouchez et al., 1983; Schmid and Casey, 1986). The clockwise and anticlockwise rotation results from the different sample orientation during CPO measurements. The asymmetry indicates, for the given orientation of the samples, a dextral strike-slip sense of shear during $D_3$ also deduced from the 'classical' shear sense indicators (Kolb et al., 2004).

### 7.2. Progressive $D_3$ deformation of laminated quartz veins

The slight dextral asymmetry of the CPO together with the microfabrics of the altered host rocks suggests a contribution by non-coaxial deformation. If the crystallographic ⟨a⟩ direction is the dominant slip direction, the *a*-axis pole figures are characteristic for distinguishing between coaxial and non-coaxial deformation (Bouchez, 1978; Lister and Dornsiepen, 1982; Schmid and Casey, 1986). The Hutti samples do not show a clear single maximum for the *a*-axis distribution (Fig. 7). Instead, the pole figures exhibit a girdle-like pattern with one intense maximum near *X* (e.g. IH 1, IH 32, IH 59). Additionally, the pole figures for the rhombohedral planes show symmetry with respect to the axis of shortening and (001) poles have a tendency to form small circles around *Z* (e.g. IH 1, IH 32, IH 29). This points to a mixed characteristic of deformation with a dominating coaxial component and a weak contribution by a non-coaxial component (Lister and Dornsiepen, 1982; Schmid and Casey, 1986).

The grain shape analysis of $quartz_1$ porphyroclasts shows that the aspect ratios in *XZ* and *YZ* sections overlap and the angle between the long axis and the *X* and *Y* directions is generally small (Figs. 4 and 5). Pyrrhotite is elongated parallel to the *X* and *Y* directions, respectively. Scheelite and quartz from sample IH 54 have overlapping aspect ratios in *XZ* and *YZ* sections. These oblate grain shapes cannot be used to quantify 2D strain, because (1) the initial grain shape is not known, (2) the grains have strongly serrated grain boundaries, and (3) the porphyroclasts are recrystallized. The quartz CPO together with the oblate grain shape of quartz, pyrrhotite, and scheelite, however, may consistently be explained by dominant coaxial deformation of the laminated quartz veins. The asymmetry of the pole figure from sample IH 59 and the different aspect ratios in *XZ* and *YZ* sections, which can also be observed in sample IH 1 (Figs. 4 and 5), point to a reactivation during progressive, possibly non-coaxial $D_3$ deformation.

### 7.3. Microstructures and textures developed during the fault-valve process

The fault-valve process involves fluid pressure and shear stress fluctuations in a shear zone system at a relatively low differential stress (Sibson et al., 1988; Boullier and Robert, 1992; Cox, 1995; Robert et al., 1995; Nguyen et al., 1998). Fluid over-pressurization results in failure, which creates the fracture permeability for fluid draining and shear vein formation. Repetition of the fluid pressurization and rupturing cycle is invoked to account for the multiple events of vein opening, filling and reactivation during coseismic and interseismic deformation stages (Sibson et al., 1988; Boullier and Robert, 1992; Sibson, 2001; Kolb et al., 2004).

The microstructures and textures of quartz veins and wall rocks can be placed into various stages of such a coseismic–interseismic cycle during fault-valve behavior of the auriferous shear zones at Hutti. The coseismic stages are represented by the formation of hydraulic breccia, fault gouge, and quartz veins (Kolb et al., 2004). The shear stress and fluid pressure release immediately following the coseismic stage has important implications on the local stress conditions. At low differential and shear stress conditions, the effective mean stress will be oriented sub-perpendicular to the shear veins. In the laminated quartz veins, the quartz texture and microstructure point to dominating coaxial ductile deformation, which is supported by the oblate grain shape of scheelite and pyrrhotite. The quartz texture and microstructure are, therefore, consistent with dominant shortening normal to the shear veins, which should be expected immediately after hydraulic fracturing, resulting from shear stress and fluid pressure release. Similarly, shortening normal to auriferous extension veins was described by Cox et al. (1991) and Boullier and Robert (1992). The relatively small grain size of some of the $quartz_2$ grains in reactivated quartz veins can possibly be explained by quartz recrystallization at high strain rates during the coseismic stage of the fault valve cycle.

Ductile creep in the shear zone rocks is manifested by the formation of S–C′ fabrics, the shear bands of the $S_2$–$S_3$ crenulation cleavage and viscous deformation of phyllosilicates, quartz, and calcite during the interseismic stages (Kolb et al., 2004). These fabrics together with the strong mineral stretching lineation point to dominant non-coaxial deformation. The fact that non-coaxial fabrics are only weakly developed in quartz veins (possibly IH 1 and IH 59) suggests strain partitioning. At the given conditions, the quartz veins were rheologically stronger than the surrounding altered wall rocks, which resulted in preferential ductile non-coaxial deformation of the phyllosilicate-rich lithology. This ductile deformation occurred in response to increased shear stress during the readjustment of the oblique, regional stress field. A reactivation of the quartz vein represented by sample IH 59 with a reoriented stress field is suggested by the asymmetry in the quartz texture. In the fault-valve

process, the recovery of shear stress is coeval with increasing fluid pressure up to supralithostatic levels due to sealing of the porosities in the shear zone. The fluid inclusion record from the laminated quartz veins at Hutti shows that fluids were pressurized up to 320 MPa (Pal and Mishra, 2002; Pandalai et al., 2003; Rogers, 2004), which might have resulted in hydraulic fracturing. The cyclic repetition of this fault-valve behavior is indicated by fracturing and ductile deformation of quartz veins and the development of the laminated quartz vein systems.

## 8. Conclusions

The auriferous laminated quartz veins at Hutti are the result of hydraulic fracturing during the greenschist facies reactivation ($D_3$) of an amphibolite facies shear zone ($D_2$) by fault-valve action in a dextral strike-slip regime. Quartz microstructures and textures from $D_2$ quartz veins show a marked greenschist facies overprint, obliterating most of the information of the earlier, amphibolite facies $D_2$ deformation event. The microstructures and textures of quartz in the laminated quartz veins are representative of the progressive greenschist facies $D_3$ deformation at 300–400 °C. The oblate shape of quartz$_1$ and scheelite$_1$ porphyroclasts and pyrrhotite in the quartz shear veins together with the symmetry of quartz textures with respect to the maximum shortening direction point to coaxial deformation perpendicular to the vein walls. Shear stress and fluid pressure release immediately after the seismic event resulted in a stress field perturbation, whereby the effective mean stress was oriented sub-perpendicular to the shear veins. Non-coaxial deformation of the veins is only weak, which points to strain partitioning into the rheologically weaker phyllosilicate-rich selvages along with shear stress and fluid pressure build-up during the progressive interseismic stage of the fault-valve cycle.

The quartz microstructures and textures in the auriferous veins provide, thus, an excellent record of fault-valve activity in a greenschist facies, dextral strike-slip shear zone. They show that the fluid pressure and shear stress recovery phase of the fault-valve cycle is not only characterized by non-coaxial ductile deformation, but also by a strong coaxial component normal to the shear veins. This study emphasizes the importance of microstructures and CPO in analyzing deformation processes, and provides new insight into seismically active, auriferous shear zones, which are important hosts for Archaean lode-gold mineralization.

## Acknowledgements

The authors would like to thank the mine management of the Hutti Gold Mine Ltd for the permission to publish the results of this study. B. Mishra and N. Pal are thanked for fruitful discussions in the field. D. Möwert, T. Derichs and M. Wiechert helped with the quartz measurements, the preparation of thin sections and photographs. M. Crumbach from the Institute of Physical Metallurgy and Metal Physics, RWTH Aachen University, is thanked for the texture measurements. Thorough reviews from G. Zulauf and an anonymous reviewer helped greatly to improve the manuscript. This study was made possible through grant Me 1425/5-1/2 of the Deutsche Forschungsgemeinschaft.

## References

Blacic, J.D., 1975. Plastic-deformation mechanisms in quartz: the effect of water. Tectonophysics 27, 271–294.

Bouchez, J.L., 1978. Preferred orientations of quartz a axes in some tectonites: kinematic inferences. Tectonophysics 49, 25–30.

Bouchez, J.L., Pêcher, A., 1981. The Himalayan main central thrust pile and its quartz-rich tectonites in Central Nepal. Tectonophysics 78, 23–50.

Bouchez, J.L., Lister, G.S., Nicolas, A., 1983. Fabric asymmetry and shear sense in movement zones. Geologische Rundschau 72, 401–419.

Boullier, A.-M., Robert, F., 1992. Palaeoseismic events recorded in Archaean gold–quartz vein networks, Val d'Or, Abitibi, Quebec, Canada. Journal of Structural Geology 14, 161–179.

Cox, S.F., 1995. Faulting processes at high fluid pressures: an example of fault-valve behavior from the Wattle Gully Fault, Victoria, Australia. Journal of Geophysical Research 100, 841–859.

Cox, S.F., Etheridge, M.A., Wall, V.J., 1986. The role of fluids in syntectonic mass transport, and the localization of metamorphic vein-type ore deposits. Ore Geology Reviews 2, 65–86.

Cox, S.F., Wall, V.J., Etheridge, M.A., Porter, T.F., 1991. Deformational and metamorphic processes in the formation of mesothermal vein-hosted gold deposits—examples from the Lachlan Fold Belt in central Victoria. Ore Geology Reviews 6, 391–423.

Cox, S.F., Knackstedt, M.A., Braun, J., 2001. Principles of structural control on permeability and fluid flow in hydrothermal systems. In: Richards, J.P., Tosdal, R.M. (Eds.), Structural Controls on Ore Genesis 14 Reviews in Economic Geology, pp. 1–24.

Drury, M.R., Urai, J.L., 1990. Deformation-related recrystallization processes. Tectonophysics 172, 235–253.

Drury, M.R., Humphreys, F.J., White, S.H., 1985. Large strain deformation studies using polycrystalline magnesium as a rock analogue. Part II: dynamic recrystallisation mechanisms at high temperatures. Physics of the Earth and Planetary Interiors 40, 208–222.

FitzGerald, J.D., Boland, J.N., McLaren, A.C., Ord, A., Hobbs, B.E., 1991. Microstructures in water-weakened single crystals of quartz. Journal of Geophysical Research 96, 2139–2155.

Heilbronner, R., Bruhn, D., 1998. The influence of three-dimensional grain size distributions on the rheology of polyphase rocks. Journal of Structural Geology 20, 695–705.

Joy, S., Saha, D., 1998. Influence of micaceous impurity on dynamically recrystallized quartz c-axis fabric in L–S tectonites from the Singhbhum Shear Zone and its footwall, Eastern India. Journal of Structural Geology 20, 1509–1520.

Joy, S., Saha, D., 2000. Dynamically recrystallized quartz c-axis fabrics in greenschist facies quartzites, Singhbhum shear zone and its footwall, eastern India - influence of high fluid activity. Journal of Structural Geology 22, 777–793.

Kolb, J., Kisters, A.F.M., Meyer, F.M., Siemes, H., 2003. Polyphase deformation of mylonites of the Renco gold mine, Northern Marginal Zone, Limpopo Belt, Zimbabwe: identified by crystallographic preferred orientation of quartz. Journal of Structural Geology 25, 253–262.

Kolb, J., Rogers, A., Meyer, F.M., Vennemann, T.W., 2004. Development of fluid conduits in the auriferous shear zones of the Hutti Gold Mine, India: evidence for spatially and temporally heterogeneous fluid flow. Tectonophysics 378, 65–84.

Kolb, J., Rogers, A., Meyer, F.M., 2005. Relative timing of deformation and two-stage gold mineralization at Hutti mine, Dharwar Craton, India. Mineralium Deposita. doi:10.1007/s00126-005-0475-y.

Kruhl, J.H., 1996. Prism- and basal-plane parallel subgrain boundaries in quartz: a microstructural geothermobarometer. Journal of Metamorphic Geology 14, 581–589.

Lister, G.S., 1977. Discussion: crossed girdle c-axis fabrics in quartzites plastically deformed by plane strain and progressive simple shear. Tectonophysics 39, 51–54.

Lister, G.S., Dornsiepen, U.F., 1982. Fabric transitions in the Saxony granulite terrain. Journal of Structural Geology 4, 81–92.

Lister, G.S., Price, G.P., 1978. Fabric development in a quartz–feldspar mylonite. Tectonophysics 49, 37–78.

Lister, G.S., Snoke, A.W., 1984. S–C mylonites. Journal of Structural Geology 6, 617–638.

Lloyd, G.E., Freeman, B., 1994. Dynamic recrystallization of quartz under greenschist facies conditions. Journal of Structural Geology 16, 867–881.

Mancktelow, N.S., Pennacchioni, G., 2004. The influence of grain boundary fluids on the microstructure of quartz–feldspar mylonites. Journal of Structural Geology 26, 47–69.

McCuaig, T.C., Kerrich, R., 1998. P–T–t deformation fluid characteristics of lode-gold deposits: evidence from alteration systematics. Ore Geology Reviews 12, 381–453.

Naganna, C., 1987. Gold mineralization in the Hutti mining area, Karnataka, India. Economic Geology 82, 2008–2016.

Nguyen, P.T., Cox, S.F., Harris, L.B., Powell, C.M., 1998. Fault-valve behaviour in optimally oriented shear zones: an example at the Revenge gold mine, Kambalda, Western Australia. Journal of Structural Geology 20, 1625–1640.

Pal, N., Mishra, B., 2002. Alteration geochemistry and fluid inclusion characteristics of the greenstone-hosted gold deposit of Hutti, Eastern Dharwar Craton, India. Mineralium Deposita 37, 722–736.

Pandalai, H.S., Jadhav, G.N., Mathew, B., Panchapakesan, V., Raju, K.K., Patil, M.L., 2003. Dissolution channels in quartz and the role of pressure changes in gold and sulfide deposition in the Archean, greenstone-hosted, Hutti gold deposit, Karnataka, India. Mineralium Deposita 38, 597–624.

Pryer, L.L., 1993. Microstructures in feldspars from a major crustal thrust zone: the Grenville Front, Ontario, Canada. Journal of Structural Geology 15, 21–36.

Riyaz Ulla, M.S., Pathan, A.M., Maaskant, P., 1996. The characterization of metamorphic facies of metabasalts of Hutti Greenstone Belt. Journal of the Geological Society of India 47, 547–554.

Robert, F., Poulsen, K.H., 2001. Vein formation and deformation in greenstone gold deposits. In: Richards, J.P., Tosdal, R.M. (Eds.), Structural Controls on Ore Genesis 14 Reviews in Economic Geology, pp. 111–155.

Robert, F., Boullier, A.-M., Firdaous, K., 1995. Gold–quartz veins in metamorphic terranes and their bearing on the role of fluids in faulting. Journal of Geophysical Research 100, 12861–12879.

Rogers, A., 2004. Petrological, Geochemical and Stable Isotope Characterisation of Auriferous Shear Zones at the Hutti Gold Mine, Dharwar Craton, India. Fachgruppe Geowissenschaften der RWTH Aachen, Aachen.

Roy, A., 1979. Polyphase folding deformation in the Hutti–Maski schist belt, Karnataka. Journal of the Geological Society of India 20, 598–607.

Rutter, E.H., Brodie, K.H., 2004. Experimental intracrystalline plastic flow in hot-pressed synthetic quartzite prepared from Brazilian quartz crystals. Journal of Structural Geology 26, 259–270.

Schaeben, H., Siemes, H., 1996. Determination and interpretation of preferred orientation with texture goniometry: an application of indicators to maximum entropy pole- to orientation-density inversion. Mathematical Geology 28, 169–201.

Schmid, S.M., Casey, M., 1986. Complete fabric analysis of some commonly observed quartz c-axis patterns. Geophysical Monographs 36, 263–286.

Sibson, R.H., 1986. Brecciation processes in fault zones: inferences from earthquake rupturing. Pure Applied Geophysics 124, 159–174.

Sibson, R.H., 1990. Faulting and fluid flow. In: Nesbitt, B.E. (Ed.), Short Course on Fluids in Tectonically Active Regimes of the Continental Crust 18 MAC Short Course Handbook, Vancouver, pp. 93–129.

Sibson, R.H., 2001. Seismogenic framework for hydrothermal transport and ore deposition. In: Richards, J.P., Tosdal, R.M. (Eds.), Structural Controls on Ore Genesis 14 Reviews in Economic Geology, pp. 25–50.

Sibson, R.H., Robert, F., Poulsen, K.H., 1988. High-angle reverse faults, fluid pressure cycling and mesothermal gold–quartz deposits. Geology 16, 551–555.

Srikantia, S.V., 1995. Geology of the Hutti–Maski greenstone belt. In: Curtis, L.C., Radhakrishna, B.P. (Eds.), Hutti Gold Mine into the 21st Century. Geological Society of India, pp. 8–27.

Stipp, M., Stünitz, H., Heilbronner, R., Schmid, S.M., 2002. The eastern Tonale fault zone: a 'natural laboratory' for crystal plastic deformation of quartz over a temperature range from 250 to 700 °C. Journal of Structural Geology 24, 1861–1884.

Traas, C., Siemes, H., Schaeben, H., 1994. Smoothing pole figures using tensor products of trigonometric and polynomial splines. Materials Science Forum 157–162, 453–458.

Vasudev, V.N., Chadwick, B., Nutman, A.P., Hedge, G.V., 2000. Rapid development of the Late Archaean Hutti schist belt, northern Karnataka: implications of new field data and SHRIMP U/Pb zircon ages. Journal of the Geological Society of India 55, 529–540.

Voll, G., 1976. Recrystallization of quartz, biotite and feldspars from Erstfeld to the Leventina Nappe, Swiss Alps, and its geological significance. Schweizerische Mineralogisch Petrograpghische Mitteilungen 56, 641–647.

Wenk, H.-R., 1994. Preferred orientation patterns in deformed quartzites. In: Heaney, P.J., Prewitt, C.T., Gibbs, G.V. (Eds.), Silica: physical behaviour, geochemistry and materials applications. Reviews in Mineralogy, pp. 177–208.

Zulauf, G., 2001. Structural style, deformation mechanisms and paleodifferential stress along an exposed crustal section: constraints on the rheology of quartzofeldspathic rocks at supra- and infrastructural levels (Bohemian Massif). Tectonophysics 332, 211–237.